INTERNATIONAL JOURNAL FOR NUMERICAL METHODS IN FLUIDS, VOL. 12, 507–533 (1991)

THREE-DIMENSIONAL HYDRODYNAMICS ON FINITE ELEMENTS. PART II: NON-LINEAR TIME-STEPPING MODEL

DANIEL R. LYNCH
Dartmouth College, Hanover, NH, U.S.A.

AND

FRANCISCO E. WERNER
Skidaway Institute of Oceanography, Savannah, GA, U.S.A.

SUMMARY

The development and application of a non-linear 3D hydrodynamic model are described. The model is based on the wave equation rearrangement of the primitive 3D shallow water equations with a general eddy viscosity formulation for the vertical shear. A Galerkin procedure is used to discretize these on simple six-node elements: linear triangles in the horizontal with linear variations in the vertical. Resolution of surface, bottom and interfacial boundary layers is facilitated and total flexibility is preserved for specifying spatial and temporal variations in the vertical viscosity and density fields. A semi-implicit time-stepping algorithm allows the solutions for elevation and velocity to be uncoupled during each time step. The elevation solution is essentially a 2D wave equation calculation with a stationary sparse matrix representing the gravity waves. With nodal quadrature the subsequent velocity calculation is achieved by factoring only a tridiagonal diffusion matrix representing the vertical viscous terms. As a result the overall calculation scales computationally as only a 2D problem but provides the full 3D solution. Application to field-scale problems is illustrated for the English Channel/Southern Bight system and the Lake Maracaibo system.

KEY WORDS Finite elements Hydrodynamics Three-dimensional hydrodynamics Non-linear hydrodynamics Tidal hydrodynamics

1. INTRODUCTION

Herein we address the motions of estuaries and coastal seas under the classical shallow water assumptions—a turbulent, incompressible, hydrostatic fluid, partially mixed vertically but effectively inviscid horizontally, driven by rotation, wind, tide and density gradients. We develop a general 3D shallow water wave equation in the time domain, show its efficient implementation on simple 3D finite elements and display some illustrative results from two field-scale simulations.

In a previous paper[1] we presented a 3D finite element model for linearized problems subject to periodic gravity and wind forcing. In that restricted context we were able to obtain general 3D solutions with an uncoupled algorithm in which the elevation is obtained by a 2D finite element calculation and the velocity profile recovered afterwards either analytically or numerically. In the numerical case the computational effort is limited to the factorization of complex tridiagonal matrices beneath each horizontal node. The overall computational effort therefore scales only as a

0271–2091/91/060507–27$13.50

Received 8 December 1989
Revised 29 March 1990

2D scalar problem. Further, the elevation solution may be obtained with any 2D harmonic shallow water code, with straightforward modifications to incorporate the vertical structure and bottom stress—in effect, one solves an equivalent 2D problem with modified bottom stress, Coriolis and wind stress parameters which depend on the distribution of vertical eddy viscosity and bottom slip coefficient. An extension of this method[2] allows the incorporation of baroclinic forcing for diagnostic purposes. Our objective in this paper is to develop a time-stepping algorithm with analogous structure and benefits for the general case of non-linear, aperiodic motions.

The linearized equations contain no horizontal gradients of velocity at depth. As a result the horizontal and vertical behaviour can be completely uncoupled and one can construct and interpret 3D solutions with only a 2D finite element mesh. With the full non-linear equations the presence of spatial gradients at depth demands a full 3D mesh. Below we show, however, that with the proper formulation, mesh selection and solution algorithm the effective uncoupling of vertical and horizontal modes may still be achieved, such that programs for mesh generation and postprocessing, as well as the solution algorithm itself, may still be built effectively within the 2D paradigm, with 1D extensions for the vertical.

The wave equation approach which we utilize was developed originally for the 2D vertically averaged shallow water equations.[3] Its implementation on finite elements has proven efficient, accurate and free of parasitic wrinkles which have historically infected finite element studies in this arena. In particular, the wave equation is effective on the simplest linear triangles without recourse to artificial viscosity or other smoothing mechanisms. Most recently, a field-scale simulation exercise has been completed in the English Channel/Southern Bight[4] in which (a) simulations of 190-day duration were successfully computed,[5] (b) results of implicit[5] and explicit[6] time-stepping as well as harmonic[7,14] calculations have agreed with each other and with conventional finite difference models[8] and (c) a reasonable fit with field data was obtained without calibration. We are thus encouraged to pursue the 3D extensions and to do so in a general way which allows the simulation of both layered and continuously stratified systems. We limit this presentation to simple eddy viscosity closure for the vertical mixing but preserve full flexibility for later incorporation of turbulence energy closure. In the same spirit we focus on the hydrodynamic response to externally specified density fields.

An additional feature of the finite element implementation of the wave equation formulation is that mass matrix diagonalization may be defensibly achieved via 'nodal quadrature'—i.e. use of spatial integration formulae in which the quadrature points coincide exactly with the nodes.* This has enabled very effective simulations on the simplest linear elements. Both harmonic and implicit time-stepping solutions can be achieved with a sparse matrix factorization of the depth matrix alone, the subsequent velocity calculations being explicit owing to the diagonal mass matrix. In the explicit time-stepping case both depth and velocity may be calculated explicitly. These are properties which have historically been enjoyed by finite difference methods and their successful implementation on finite elements is very desirable. We strive to preserve these properties in adding the vertical dimension.

Overall, we find that a very effective, complete 3D hydrodynamic model may be constructed by judiciously combining the progress achieved in 2D time stepping with 3D extensions in the general spirit of our harmonic model. The use of the wave equation eliminates the problem of spurious gravity waves on simple elements; a semi-implicit time-stepping scheme uncouples the elevation

* It is important to note that this quadrature rule is applied to *all* terms in *each* weighted residual expression, not arbitrarily to the mass matrix alone.

from the velocity in each time step; and the use of nodal quadrature renders the momentum equation tridiagonal on simple elements. The use of simple elements simplifies the algorithm and its future extensions and can significantly reduce the computational overhead in pre- and postprocessing.

2. GOVERNING EQUATIONS

We solve the 3D hydrodynamic equations with the conventional Boussinesq and hydrostatic assumptions. There are no horizontal shear stresses and a general eddy viscosity formulation is used to represent the vertical shear stress. The vertical viscosity and density field are assumed to be time- and space-dependent with no restrictions on their functional dependence. Using the following notation,

$\mathbf{v}(x, y, z, t)$	fluid velocity, with Cartesian components (u, v, w)
$\zeta(x, y, t)$	free surface elevation
$h(x, y)$	bathymetric depth
$H(x, y, t)$	total fluid depth, $H = h + \zeta$
$N(x, y, z, t)$	vertical eddy viscosity
$\rho(x, y, z, t)$	fluid density
g	gravity
$\mathbf{f}$	Coriolis vector, directed vertically
∇	gradient operator
∇_{xy}	horizontal gradient operator
(x, y)	horizontal Cartesian co-ordinates
z	vertical co-ordinate, positive upward, $-h \leqslant z \leqslant \zeta$
t	time,

we write the 3D equations for continuity,

$$\nabla \cdot \mathbf{v} = 0, \tag{1}$$

and horizontal momentum,

$$\frac{\partial \mathbf{v}}{\partial t} + \mathbf{v} \cdot \nabla \mathbf{v} + g \nabla_{xy} \zeta + \mathbf{f} \times \mathbf{v} - \frac{\partial}{\partial z}\left(N \frac{\partial \mathbf{v}}{\partial z} \right) = \mathbf{R}, \tag{2}$$

where $\mathbf{R}$ is the baroclinic pressure gradient:

$$\mathbf{R}(x, y, z, t) = -\frac{g}{\rho_0} \int_z^\zeta \nabla_{xy} \rho \, dz. \tag{3}$$

The depth-averaged forms of equations (1) and (2) are

$$\frac{\partial H}{\partial t} + \nabla_{xy} \cdot H \bar{\mathbf{v}} = 0, \tag{4}$$

$$\frac{\partial H \bar{\mathbf{v}}}{\partial t} + \nabla_{xy} \cdot (H \overline{\mathbf{v}\mathbf{v}}) + g H \nabla_{xy} \zeta + \mathbf{f} \times H \bar{\mathbf{v}} - N \frac{\partial \mathbf{v}}{\partial z}\bigg|_{z=\zeta} + N \frac{\partial \mathbf{v}}{\partial z}\bigg|_{z=-h} = H \bar{\mathbf{R}}, \tag{5}$$

where the overbar indicates a vertically averaged quantity. We rearrange the latter two equations to obtain the shallow water wave equation in three steps: (a) differentiate (4) with respect to time; (b) eliminate $\partial H \bar{\mathbf{v}}/\partial t$ using (5); (c) add equation (4) weighted by a constant τ_0. The result is the

shallow water wave equation:

$$\frac{\partial^2 H}{\partial t^2}+\tau_0\frac{\partial H}{\partial t}-\nabla_{xy}\cdot\left[\nabla_{xy}\cdot(H\overline{\mathbf{v}\mathbf{v}})+gH\nabla_{xy}\zeta+\mathbf{f}\times H\bar{\mathbf{v}}-\tau_0 H\bar{\mathbf{v}}-N\frac{\partial \mathbf{v}}{\partial z}\bigg|_{z=\zeta}+N\frac{\partial \mathbf{v}}{\partial z}\bigg|_{z=-h}-H\bar{\mathbf{R}}\right]=0. \tag{6}$$

In this 3D version there are two notable departures relative to the usual 2D version:[5] both the bottom stress and the vertical average of the momentum convection terms are preserved in their exact 3D form. The expression of these in terms of the actual, instantaneous 3D velocity profile rather than in terms of its vertical average is of course one of the goals of 3D modelling.

We solve these equations subject to conventional horizontal boundary conditions on depth or normal transport, and to vertical boundary conditions on shear stress. At the surface we enforce the atmospheric shear stress:

$$N\frac{\partial \mathbf{v}}{\partial z}\bigg|_{z=\zeta}=H\boldsymbol{\Psi}. \tag{7a}$$

At the bottom we use a conventional slip condition relating shear to the bottom velocity:

$$N\frac{\partial \mathbf{v}}{\partial z}\bigg|_{z=-h}=H\boldsymbol{\Gamma}(\mathbf{v}_b), \tag{7b}$$

in which $\boldsymbol{\Gamma}$ is a general non-linear function of the bottom velocity $\mathbf{v}_b$. Inserting (7a, b) into (6), we arrive at the final form of the wave equation:

$$\frac{\partial^2 H}{\partial t^2}+\tau_0\frac{\partial H}{\partial t}-\nabla_{xy}\cdot[\nabla_{xy}\cdot(H\overline{\mathbf{v}\mathbf{v}})+gH\nabla_{xy}\zeta+\mathbf{f}\times H\bar{\mathbf{v}}-\tau_0 H\bar{\mathbf{v}}-H\boldsymbol{\Psi}+H\boldsymbol{\Gamma}-H\bar{\mathbf{R}}]=0. \tag{8}$$

We solve (8) for ζ, (2) for the horizontal components of $\mathbf{v}$ and (1) for the vertical velocity w.

3. THREE-DIMENSIONAL ELEMENTS

We have pursued the simplest general approach to the vertical: linear finite elements. These provide the full geometric flexibility associated with the finite element method, close no options with respect to the incorporation of baroclinic motions and turbulent closure, and establish a baseline against which more complicated elements may be tested.

A design principle at the outset has been operational simplicity and we have sought to exploit as much as possible the nearly 2D structure of the equations and the existing body of 2D pre- and postprocessing software. As a result we have investigated the six-node elements illustrated conceptually in Figure 1, arranged in a stack of topologically identical layers of varying thickness. *These elements admit nodal quadrature*—i.e. use of quadrature points coincident with the nodes will exactly integrate their volume. We are careful to require that *nodes line up perfectly in the vertical.* The operational gain in mesh generation is clear—only one 2D mesh need be generated, based on conventional criteria related to local depth and horizontal geometry, and the vertical dimension can be generated analytically on the basis of separate time-dependent criteria. In addition, the combination of the vertical alignment with nodal quadrature renders the momentum calculations *tridiagonal*, with obvious practical implications (see below). Finally, we allow *nodes* to *move vertically* in order to track internal interfaces as well as the free surface and to accommodate the general evolution of the viscosity structure.

Interpolation of the dependent variables is achieved on the mapped version of the mesh shown on the right side of Figure 1. The mapping from the native (x, y, z) system into the local system

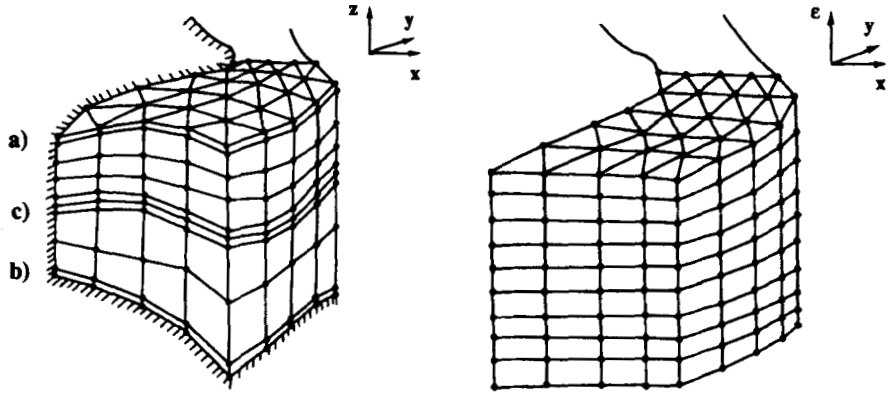

Figure 1. Main features of the layered mesh: element sides perfectly vertical; variable mesh spacing to resolve boundary and internal layers (a, b, c); uniform mesh spacing in mapped (x, y, ε) system; nodes free to move vertically to track (a) free surface and (c) internal fronts; all layers have identical topology; $\nabla_{xy|\varepsilon}$ invariant with depth

(x, y, ε) leaves the horizontal co-ordinates unchanged; the vertical mapping is isoparametric:

$$z(x, y, \varepsilon, t) = \sum_i z_i(t)\,\phi_i(x, y, \varepsilon). \tag{9}$$

Here $z_i(t)$ is the time-dependent vertical location of node i and ϕ_i are the basis functions used to expand the velocity solution:

$$\mathbf{v}(x, y, \varepsilon, t) = \sum_i \mathbf{v}_i(t)\,\phi_i(x, y, \varepsilon). \tag{10}$$

Derivatives with respect to z are straightforward in the local co-ordinate system; the other derivatives are slightly complicated by the time-dependent mapping:

$$\left.\frac{\partial}{\partial t}\right|_{x,y,z} = \left(\frac{\mathrm{D}}{\mathrm{D}t} - w_{\mathrm{mesh}}\frac{\partial}{\partial z}\right)\Bigg|_{x,y,\varepsilon}, \tag{11}$$

$$\left.\frac{\partial}{\partial x}\right|_{x,y,z} = \left(\frac{\partial}{\partial x} - \frac{\partial z}{\partial x}\frac{\partial}{\partial z}\right)\Bigg|_{x,y,\varepsilon}, \tag{12}$$

$$\left.\frac{\partial}{\partial y}\right|_{x,y,z} = \left(\frac{\partial}{\partial y} - \frac{\partial z}{\partial y}\frac{\partial}{\partial z}\right)\Bigg|_{x,y,\varepsilon}, \tag{13}$$

where D/Dt indicates differentiation following the motion of the *mesh* and where

$$w_{\mathrm{mesh}} \equiv \left.\frac{\partial z}{\partial t}\right|_{x,y,\varepsilon} = \sum \frac{\mathrm{d}z_i}{\mathrm{d}t}\phi_i \equiv \frac{\mathrm{D}z}{\mathrm{D}t} \tag{14}$$

is the vertical motion of the mesh. The derivative D/Dt is the natural time derivative for quantities expanded in the (x, y, ε) basis. For example, from (10),

$$\frac{\mathrm{D}\mathbf{v}}{\mathrm{D}t} = \sum_i \frac{\mathrm{d}\mathbf{v}_i}{\mathrm{d}t}\phi_i. \tag{15}$$

Substitution of these transformations into the momentum equation yields, in the (x, y, ε) system,

$$\frac{\mathbf{Dv}}{\mathrm{D}t}+\mathbf{v}\cdot\nabla_{xy|\varepsilon}\mathbf{v}+F\frac{\partial \mathbf{v}}{\partial z}+g\nabla_{xy}\zeta+\mathbf{f}\times\mathbf{v}-\frac{\partial}{\partial z}\left(N\frac{\partial \mathbf{v}}{\partial z}\right)=\mathbf{R}, \tag{16}$$

in which $\nabla_{xy|\varepsilon}$ is the horizontal gradient holding ε constant, and

$$F=w-w_{\text{mesh}}-\mathbf{v}\cdot\nabla_{xy|\varepsilon}z. \tag{17}$$

The quantity F is exactly the flux through the surface $\varepsilon=$constant. Where it is desirable to track material surfaces within the fluid, $F=0$ and the momentum equation is especially simple. In these cases $F=0$ prescribes the value of w_{mesh}:

$$w_{\text{mesh}}=w-\mathbf{v}\cdot\nabla_{xy|\varepsilon}z. \tag{18}$$

Alternatively, we may wish to dictate the mesh motion—for example, in a boundary layer we may require a surface of constant $\sigma=(z-\zeta)/H$,

$$w_{\text{mesh}}=(\sigma+1)\frac{\partial \zeta}{\partial t}, \tag{19}$$

or constant z,

$$w_{\text{mesh}}=0. \tag{20}$$

In such cases where w_{mesh} is given, F may be computed from (17). The continuity equation is similarly transformed in the (x, y, ε) system:

$$\frac{\partial w}{\partial z}=-\nabla_{xy|\varepsilon}\cdot\mathbf{v}+\frac{\partial \mathbf{v}}{\partial z}\cdot\nabla_{xy|\varepsilon}z \tag{21}$$

The wave equation (8) is of course unaffected by these transformations.

A final point relative to the mesh in Figure 1 is that the numerous horizontal gradient operations in the transformed equations are invariant with depth and time, with attendant economy in equation assembly. These are facilitated by re-expressing the basis in equivalent form with the horizontal and vertical variations separated:

$$\phi_{ij}(x, y, \varepsilon)=W_i(x, y)E_j(\varepsilon), \tag{22}$$

where the double subscripts (i, j) refer to horizontal and vertical positions in the mesh, W_i are the standard linear triangular bases in the horizontal plane and E_j are the 1D chapeau functions in the vertical. In this notation it is clear that $\nabla_{xy|\varepsilon}\phi_{ij}$ is the familiar $\nabla_{xy}W_i$ in the plane, here depth-invariant, and the Jacobi determinant $|J|$ at any 3D point is simply Δz, the local vertical height of the element.

4. DISCRETIZATION AND SOLUTION PROCEDURE

Here we present a semi-implicit algorithm in which the basic linear gravity wave terms are treated in a centred, implicit manner and the depth, horizontal velocity and vertical velocity are obtained sequentially rather than simultaneously.

4.1. The depth solution

A straightforward Galerkin discretization of the wave equation is used. Note at the outset that this is a 2D equation. While we use the customary finite element notation, the 3D basis ϕ_i is

reduced to its horizontal projection W_i and all domain and boundary integrals are performed in the (x, y) plane.

The weak form which we use is a weighted residual form of (8):

$$\left\langle \frac{\partial^2 H}{\partial t^2} W_i \right\rangle + \left\langle \tau_0 \frac{\partial H}{\partial t} W_i \right\rangle + \langle [\nabla_{xy} \cdot (H\bar{\mathbf{v}}\bar{\mathbf{v}}) + gH\nabla_{xy}\zeta + \mathbf{f} \times H\bar{\mathbf{v}} - \tau_0 H\bar{\mathbf{v}} - H\bar{\boldsymbol{\Psi}} + H\bar{\boldsymbol{\Gamma}} - H\bar{\mathbf{R}}] \cdot \nabla_{xy} W_i \rangle$$

$$= -\oint \left(\frac{\partial H\bar{\mathbf{v}}}{\partial t} + \tau_0 H\bar{\mathbf{v}} \right) \cdot \hat{\mathbf{n}} W_i \, ds \tag{23}$$

where $\langle\ \rangle$ and $\oint$ represent integration over the (x, y) plane and its boundary respectively. Note that this form displays as the natural boundary condition the hydrodynamic transport $H\bar{\mathbf{v}} \cdot \hat{\mathbf{n}}$ in the boundary integral. Expansion of H and ζ in the basis W_i,

$$H(x, y, t) = \sum_j H_j(t) W_j(x, y), \tag{24a}$$

$$\zeta(x, y, t) = \sum_j \zeta_j(t) W_j(x, y), \tag{24b}$$

leads to the Galerkin form

$$\sum_j \left(\frac{d^2 H_j}{dt^2} \langle W_j W_i \rangle + \tau_0 \frac{dH_j}{dt} \langle W_j W_i \rangle + \zeta_j \langle gh\nabla_{xy} W_j \cdot \nabla_{xy} W_i \rangle \right)$$

$$= -\langle [\nabla_{xy} \cdot (H\bar{\mathbf{v}}\bar{\mathbf{v}}) + g\zeta\nabla_{xy}\zeta + \mathbf{f} \times H\bar{\mathbf{v}} - \tau_0 H\bar{\mathbf{v}} - H\bar{\boldsymbol{\Psi}} + H\bar{\boldsymbol{\Gamma}} - H\bar{\mathbf{R}}] \cdot \nabla_{xy} W_i \rangle$$

$$- \oint \left(\frac{\partial H\bar{\mathbf{v}}}{\partial t} + \tau_0 H\bar{\mathbf{v}} \right) \cdot \hat{\mathbf{n}} W_i \, ds. \tag{25}$$

(Here we have purposely split the gravity term in two and moved the non-linear part to the right side in order to render the implicit time-stepping matrix (below) stationary.)

A three-level, semi-implicit discretization is adopted in time, with the terms on the left side of (25) centred, implicit and those on the right-side centred, explicit. With the superscript k indicating the time level we define

$$\Delta H_j \equiv H_j^{k+1} - H_j^{k-1} \equiv \Delta\zeta_j \tag{26a}$$

and approximate the time derivatives by second-order differences:

$$\frac{dH_j}{dt} = \frac{\Delta H_j}{2\Delta t}, \tag{26b}$$

$$\frac{d^2 H_j}{dt^2} = \frac{H_j^{k+1} - 2H_j^k + H_j^{k-1}}{\Delta t^2} = \frac{\Delta H_j - 2(H_j^k - H_j^{k-1})}{\Delta t^2}. \tag{26c}$$

In the gravity term on the left side, ζ is implicit and centred:

$$\zeta_j = \frac{\theta}{2}(\zeta_j^{k+1} + \zeta_j^{k-1}) + (1-\theta)\zeta_j^k = \frac{\theta}{2}\Delta\zeta_j + \zeta_j^k - \theta(\zeta_j^k - \zeta_j^{k-1}). \tag{26d}$$

Substitution of these approximations into (25) and evaluation of all the right-side terms at time level k yields, after rearrangement, the linear system

$$A_{ij}\Delta H_j = r_{wi}, \tag{27a}$$

where

$$A_{ij}=\langle W_j W_i\rangle\left(1+\frac{\tau_0\Delta t}{2}\right)+\frac{\theta\Delta t^2}{2}\langle gh\nabla_{xy}W_j\cdot\nabla_{xy}W_i\rangle, \tag{27b}$$

$$r_{wi}=-\Delta t^2\langle[\nabla_{xy}\cdot(H\overline{\mathbf{vv}})+gH\nabla_{xy}\zeta+\mathbf{f}\times H\bar{\mathbf{v}}-\tau_0 H\bar{\mathbf{v}}-H\boldsymbol{\Psi}+H\boldsymbol{\Gamma}-H\bar{\mathbf{R}}]\cdot\nabla_{xy}W_i\rangle$$
$$+2\langle(H^k-H^{k-1})W_i\rangle+\theta\Delta t^2\langle gh\nabla_{xy}(\zeta^k-\zeta^{k-1})\cdot\nabla_{xy}W_i\rangle-\Delta t^2\oint\left(\frac{\partial H\bar{\mathbf{v}}}{\partial t}+\tau_0 H\bar{\mathbf{v}}\right)\cdot\hat{\mathbf{n}}W_i\,\mathrm{d}s \tag{27c}$$

and all terms without a superscript are evaluated at time level k.

We evaluate all integrals numerically with quadrature points at the nodes in all cases. As a result the matrix A_{ij} is diagonal when $\theta=0$, enabling a perfectly explicit time step for ΔH. More generally, A_{ij} is stationary, sparse, banded and symmetric. Its LU decomposition once at the beginning of a simulation allows efficient calculation of ΔH, uncoupled from the unknown velocity $\mathbf{v}^{k+1}$ during any time step. The quantities $H\overline{\mathbf{vv}}$, $H\bar{\mathbf{v}}$, $\boldsymbol{\Gamma}$, $\boldsymbol{\Psi}$ and $\bar{\mathbf{R}}$ are all obtained at time level k (with vertical integration as appropriate) at each node in the horizontal mesh and interpolated with the basis W_j.

Boundary conditions on depth are enforced exactly and the corresponding wave equation is discarded. Boundary conditions on normal transport are enforced through the boundary integral in addition to their enforcement directly on the velocity solution (see below).

Overall, this depth calculation is essentially the same as that introduced by Lynch and Gray,[3] with Kinnmark's[9] introduction of the constant factor τ_0. We have generally adopted this modification in our 2D simulations;[5,10] in fact the original[3] form in which the term $\tau\partial H/\partial t$ is introduced through the bottom stress does not apply in 3D since the bottom stress is not expressed in terms of the vertically averaged velocity.

4.2. The horizontal velocity solution

The solution for the horizontal components (u, v) of $\mathbf{v}$ is obtained by a straightforward Galerkin treatment of the momentum equation (16), with known gravity forcing at the new time level. The weak form is

$$\left\langle\left(\frac{\mathrm{D}\mathbf{v}}{\mathrm{D}t}+\mathbf{f}\times\mathbf{v}\right)\phi_i\right\rangle+\left\langle N\frac{\partial\mathbf{v}}{\partial z}\frac{\partial\phi_i}{\partial z}\right\rangle=\oint N\frac{\partial\mathbf{v}}{\partial z}\phi_i\hat{\mathbf{z}}\cdot\hat{\mathbf{n}}\,\mathrm{d}s+\left\langle\left(\mathbf{R}-g\nabla_{xy}\zeta-\mathbf{v}\cdot\nabla_{xy|\varepsilon}\mathbf{v}-F\frac{\partial\mathbf{v}}{\partial z}\right)\phi_i\right\rangle, \tag{28}$$

in which $\langle\ \rangle$ and $\oint$ denote the 3D volume and boundary integrals. Note that the natural boundary conditions on shear stress appear in the latter integral; this is the vehicle for applying the wind and bottom stresses, equations (7a, b). The complication of the Coriolis term is removed by introducing a complex surrogate for $\mathbf{v}$, $v\equiv u+\mathrm{j}v$, where $\mathrm{j}=\sqrt{(-1)}$:

$$\left\langle\left(\frac{\mathrm{D}v}{\mathrm{D}t}+\mathrm{j}fv\right)\phi_i\right\rangle+\left\langle N\frac{\partial v}{\partial z}\frac{\partial\phi_i}{\partial z}\right\rangle=\oint N\frac{\partial v}{\partial z}\phi_i\hat{\mathbf{z}}\cdot\hat{\mathbf{n}}\,\mathrm{d}s+r_{vi}. \tag{29a}$$

Here r_{vi} combines the known baroclinic, gravity and convective terms:

$$r_{vi}=\left\langle\left(R_x-g\frac{\partial\zeta}{\partial x}-\mathbf{v}\cdot\nabla_{xy|\varepsilon}u-F\frac{\partial u}{\partial z}\right)\phi_i\right\rangle+\mathrm{j}\left\langle\left(R_y-g\frac{\partial\zeta}{\partial y}-\mathbf{v}\cdot\nabla_{xy|\varepsilon}v-F\frac{\partial v}{\partial z}\right)\phi_i\right\rangle. \tag{29b}$$

Expansion of (u, v) and therefore v in the basis ϕ_i then yields the Galerkin form

$$\sum_j\left(\langle\phi_i\phi_j\rangle\frac{\mathrm{D}v_j}{\mathrm{D}t}+\mathrm{j}f\langle\phi_i\phi_j\rangle v_j+\left\langle N\frac{\partial\phi_i}{\partial z}\frac{\partial\phi_j}{\partial z}\right\rangle v_j\right)=\oint N\frac{\partial v}{\partial z}\phi_i\hat{\mathbf{z}}\cdot\hat{\mathbf{n}}\,\mathrm{d}s+r_{vi}. \tag{30}$$

A two-level time discretization is used for momentum, with all terms centred at time level $k+\frac{1}{2}$ except for the convective terms, which are lagged at time level k for computational efficiency.* With the definition of the time-centred average

$$v_j^* \equiv \frac{v_j^{k+1}+v_j^k}{2}, \tag{31a}$$

the second-order approximation for the time derivative becomes

$$\frac{Dv_j}{Dt} = \frac{v_j^{k+1}-v_j^k}{\Delta t} = \frac{2(v_j^*-v_j^k)}{\Delta t}. \tag{31b}$$

Substitution of these approximations on the left side of (30) gives

$$\sum_j \left[\langle \phi_i \phi_j \rangle \left(\frac{2}{\Delta t} + jf \right) + \left\langle N \frac{\partial \phi_i}{\partial z} \frac{\partial \phi_j}{\partial z} \right\rangle \right] v_j^* = \oint N \frac{\partial v}{\partial z} \phi_i \hat{\mathbf{z}} \cdot \hat{\mathbf{n}} \, ds + \frac{2}{\Delta t} \langle v^k \phi_i \rangle + r_{vi}^{**}, \tag{32a}$$

in which all quantities in r_{vi}^{**} are centred except for the convective terms:

$$r_{vi}^{**} \equiv \left\langle \left(R_x - g \frac{\partial \zeta}{\partial x} \right)^* \phi_i + j \left(R_y - g \frac{\partial \zeta}{\partial y} \right)^* \phi_i \right\rangle + \left\langle \left(-\mathbf{v} \cdot \nabla_{xy|\varepsilon} u - F \frac{\partial u}{\partial z} \right)^k \phi_i + j \left(-\mathbf{v} \cdot \nabla_{xy|\varepsilon} v - F \frac{\partial v}{\partial z} \right)^k \phi_i \right\rangle. \tag{32b}$$

The use of nodal quadrature renders the mass matrix $\langle \phi_i \phi_j \rangle$ diagonal, as expected; but in addition it renders the stiffness matrix $\langle N(\partial \phi_i/\partial z)(\partial \phi_j/\partial z) \rangle$ *tridiagonal*, with algebraic connections only among nodes which share the same vertical line. This latter result is evident by inspection of Figure 2, where the vanishing of $\partial \phi_i/\partial z$ along neighbouring vertical lines is a direct consequence of the vertical alignment of the mesh. In the limiting case of constant N and Δz the tridiagonal left side of (32a) reproduces conventional second-order finite difference expressions for vertical diffusion.

Vertical stress boundary conditions are enforced through the boundary integral. At the surface known values of the wind stress $H\boldsymbol{\Psi}$ are used. At the bottom a partial slip condition is employed implicitly. In the simple linear case

$$H\boldsymbol{\Gamma}^* = \kappa \mathbf{v}^* \tag{33}$$

is used. In the more common quadratic case the quasilinear form

$$H\boldsymbol{\Gamma}^* = \kappa |\mathbf{v}^k| \mathbf{v}^{k+1} = 2\kappa |\mathbf{v}^k| \mathbf{v}^* - \kappa |\mathbf{v}^k| \mathbf{v}^k \tag{34}$$

is used. In either case the coefficient of the unknown $\mathbf{v}^*$ is embedded in the left-side matrix.

During each time step following the solution for ζ^{k+1}, the complex tridiagonal system (32) is assembled under each horizontal node and the appropriate vertical boundary conditions are applied. (Note that since the nodes move vertically, all integrals are evaluated on the mesh at the centre of the time step.) The system is then solved directly by the Thomas algorithm.[11] Horizontal boundary conditions on $\mathbf{v} \cdot \hat{\mathbf{n}}$ are then enforced directly on the solution by sacrificing the normal component of velocity computed as above in favour of the exact boundary value.

* This is analogous to current practice in 2D wave equation simulations.[5,6,9,10] An earlier 2D formulation[3] used a three-level, leapfrog momentum equation with centred, explicit convective terms. This has led to non-linear instabilities and has been abandoned.

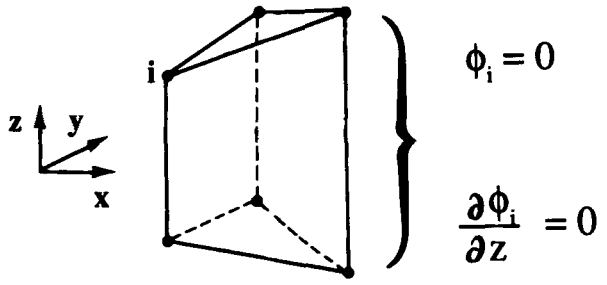

Figure 2. Six-node element with vertical sides. The features shown illustrate the tridiagonality stemming from nodal quadrature

This procedure for enforcing normal boundary conditions on velocity is exactly analogous to that used previously in 2D.[5,10] In effect the normal momentum equation is removed in favour of exact enforcement of $\mathbf{v} \cdot \hat{\mathbf{n}}$. However, the Coriolis term in the tangential momentum equation is not affected by this procedure and therefore the tangential force balance 'feels' the normal boundary condition only weakly. Exact specification of $\mathbf{v} \cdot \hat{\mathbf{n}}$ in the tangential momentum equation is easily incorporated into the tridiagonal structure with no important algorithmic consequences. Numerical experiments to date indicate negligible effect of this option, although it deserves further study.

4.3. The vertical velocity solution

Computation of the vertical velocity w is based on the continuity equation (21). We expand w in the basis ϕ_i (the same basis used for u and v) and use a weighted residual formulation combining the Galerkin method in the horizontal and the subdomain method in the vertical:

$$\sum_j \left\langle P_i \frac{\partial \phi_j}{\partial z} \right\rangle w_j = -\left\langle \left(\nabla_{xy|\varepsilon} \cdot \mathbf{v} - \frac{\partial \mathbf{v}}{\partial z} \cdot \nabla_{xy|\varepsilon} z \right) P_i \right\rangle. \tag{35}$$

Here the weighting function P_i equals the 2D linear triangular basis function W_i in the layer of elements immediately below node i and vanishes elsewhere. Equivalently in the (i, j) numbering system we have $\phi_{ij} \equiv W_i(x, y) E_j(\varepsilon)$ and $P_{ij} \equiv W_i(x, y) S_j(\varepsilon)$, with E_j the 1D chapeau functions as above and S_j a step function in the vertical. By inspection of Figure 2 one concludes that the matrix $\langle P_i \partial \phi_j / \partial z \rangle$ is of *bidiagonal* form, i.e. only one non-zero off-diagonal entry, coupling each node only with its neighbour immediately below.* The system can therefore be solved explicitly from the bottom up, beginning with the boundary condition that the bottom velocity $\mathbf{v}_b$ be parallel to the bottom:

$$w_b = -\mathbf{v}_b \cdot \nabla_{xy|\varepsilon} h \tag{36}$$

($z = -h(x, y)$ defines the bottom). Since this condition requires differentiation, we enforce it in the Galerkin sense:

$$\langle w_b W_i \rangle = -\langle (\mathbf{v}_b \cdot \nabla_{xy|\varepsilon} h) W_i \rangle, \tag{37}$$

which is explicit under nodal quadrature. No other constraints are exercised on w. In particular, the flow is allowed to slip freely at vertical sidewalls.

* Use the standard Galerkin version of (35) would produce a tridiagonal form.

During each time step following the computation of $(u, v)^{k+1}$ we assemble (35) and (37) beneath each horizontal node and solve for w^{k+1} sequentially from the bottom up. All integrals are evaluated with the mesh positioned at time level $k+1$ and the right side is similarly evaluated at time $k+1$. The remarkable outcome of the combined methods for (u, v) and w is that with the convective, gravity and bottom stress terms known the entire 3D velocity field may be computed with only tridiagonal effort.

4.4. Mesh motion

The details of mesh motion are left largely unspecified and may be tailored to specific applications. The general principles laid out in Section 3 above relate the nodal trajectories $z_i(t)$ intimately to (a) the time-dependent isoparametric mapping, essentially dictating the geometry and limits of integration for the 3D volume and surface integrals, and (b) the evaluation of spatial derivatives within the elements as in equations (16) and (17).

Operationally, a time step proceeds as follows. The computation of ζ_i^{k+1} is done first on the centred mesh at time k. This dictates the new position of the surface nodes, following which the interior node positions z_i^{k+1} are determined to suit the application. The mesh is then repositioned at $z_i^{k+1/2}$ and $w_{\text{mesh}}^{k+1/2}$ is computed as $(z_i^{k+1}-z_i^k)/\Delta t$ and used in the momentum equation which is assembled and solved at the centred time $k+\frac{1}{2}$ (with the convective terms lagged at time k). Finally, the mesh is repositioned at z_i^{k+1} to assemble and solve the continuity equation, which is evaluated entirely at time $k+1$. The sequential ordering of the calculations is shown in Table I, where it is clear that the time centring of the Galerkin equations is maintained in the evolution of the geometry as well as the hydrodynamic variables.

5. RESULTS

As a first test case we have revisited one of the linearized analytic solutions used previously in testing our harmonic model—the so-called quarter-circle test case. The problem geometry, boundary conditions and horizontal mesh appear in Figure 3 and are unchanged from Reference 1. Bathymetry varies quadratically with r: $h=h_0r^2$. The problem is driven by tidal forcing at the open boundary, with the tidal amplitude given along the open boundary as $\zeta_0=0{\cdot}1\cos(2\theta)$, setting up a 180° phase change about $\theta=45°$. To permit the use of the analytic solution, N is constant through the depth but varies with (x, y) such that N/h^2 is constant.[12] We used 10 equally spaced elements in the vertical, with linear bottom stress coefficient sufficiently large to enforce no slip at the bottom. All other non-linear terms were retained but their effects

Table I. Overview of a time step. The computation proceeds sequentially from top to bottom

Equation	Dependent variable	Basis functions	Weighting functions	Centered at	Mesh location
Wave	ζ^{k+1}	$W_i(x, y)$	$W_i(x, y)$	k	z^k
Momentum	$(u,v)^{k+1}$	$W_i(x, y)E_j(\varepsilon)$	$W_i(x, y)E_j(\varepsilon)$	$k+1/2$	$z^{k+1/2}$
Continuity	w^{k+1}	$W_i(x, y)E_j(\varepsilon)$	$W_i(x, y)S_j(\varepsilon)$	$k+1$	z^{k+1}

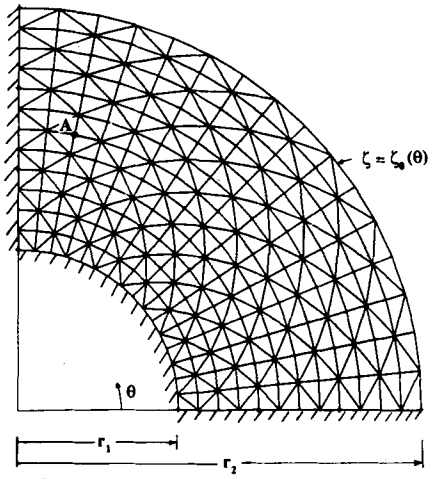

Figure 3. Analytic solution test case. There are 221 nodes and 384 elements in the horizontal. The hatched lines indicate impermeable boundaries; along $r=r_2$ the elevation time series is prescribed. Node A is sampled in Figure 7.

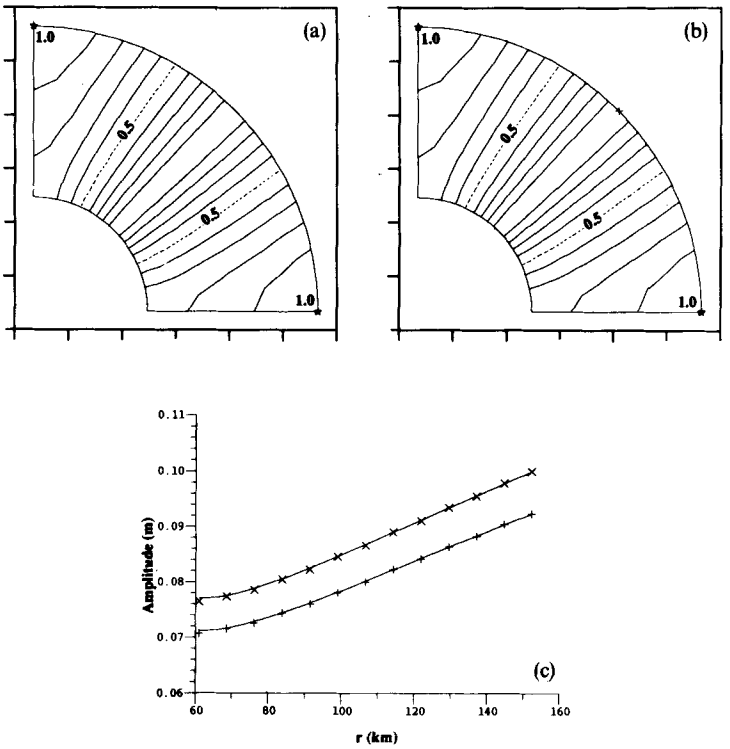

Figure 4. Tidal amplitudes in 0·01 m intervals for the test case in Figure 3: (a) normalized analytic result, interpolated on the FE grid; (b) normalized numerical result; (c) analytic (solid lines) and numerical results versus r for $\theta=0$ (+) and $\theta=\pi/16$ (×)

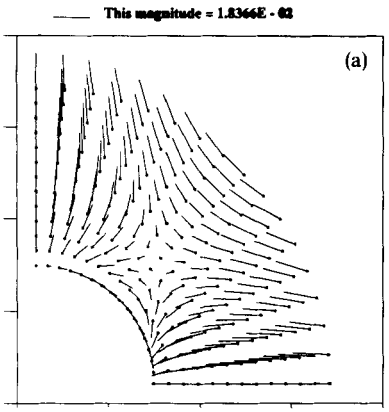

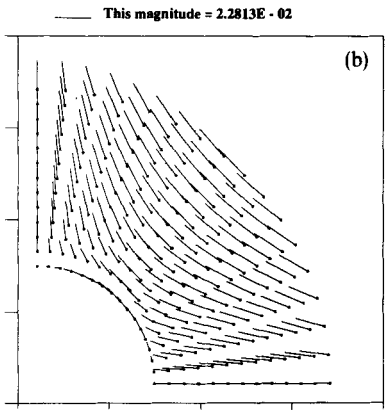

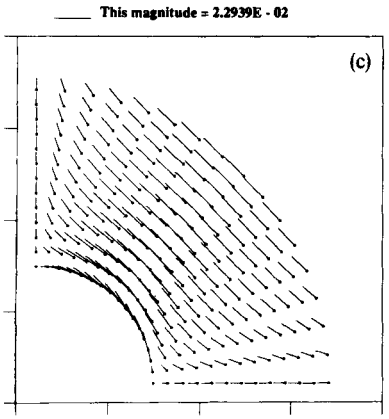

Figure 5. Numerical velocities ($m\,s^{-1}$) at $t=0$ for the test case in Figure 3: (a) surface; (b) mid-depth; (c) one level above the bottom

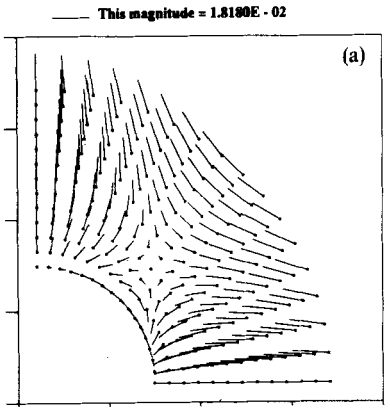

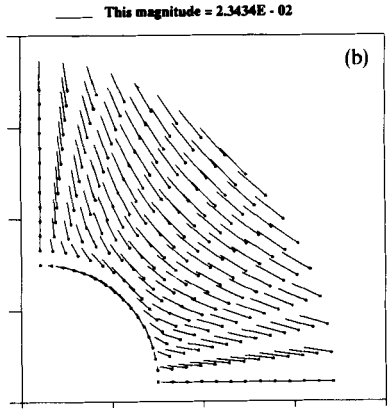

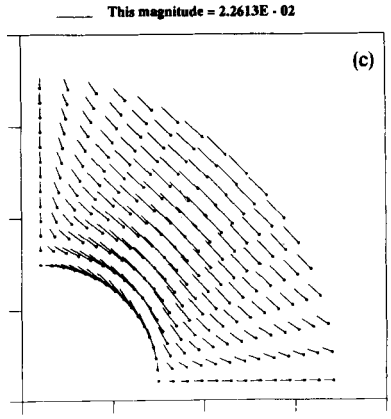

Figure 6. Analytic velocities ($m\,s^{-1}$) at $t=0$ for the test case in Figure 3: (a) surface; (b) mid-depth; (c) one level above the bottom

minimized by use of small-amplitude forcing. The physical parameters are:

$r_1 = 60\,960$ m

$r_2 = 152\,400$ m

$h_0 = 3{\cdot}048\, r_1^{-2}$ m^{-1}

$\omega = 1{\cdot}41 \times 10^{-4}$ s^{-1}

$\kappa = 10$ m s^{-1} (effectively, no slip)

$\dfrac{\omega h^2}{N} = 10$

$\mathbf{f} = 0.$

The computed elevation is displayed with the analytic result in Figure 4; Figures 5 and 6 show velocity plots at three different constant-ε levels; and Figure 7 shows the velocity as a function of depth at mesh point A. In all cases the agreement with the analytic solution is excellent and

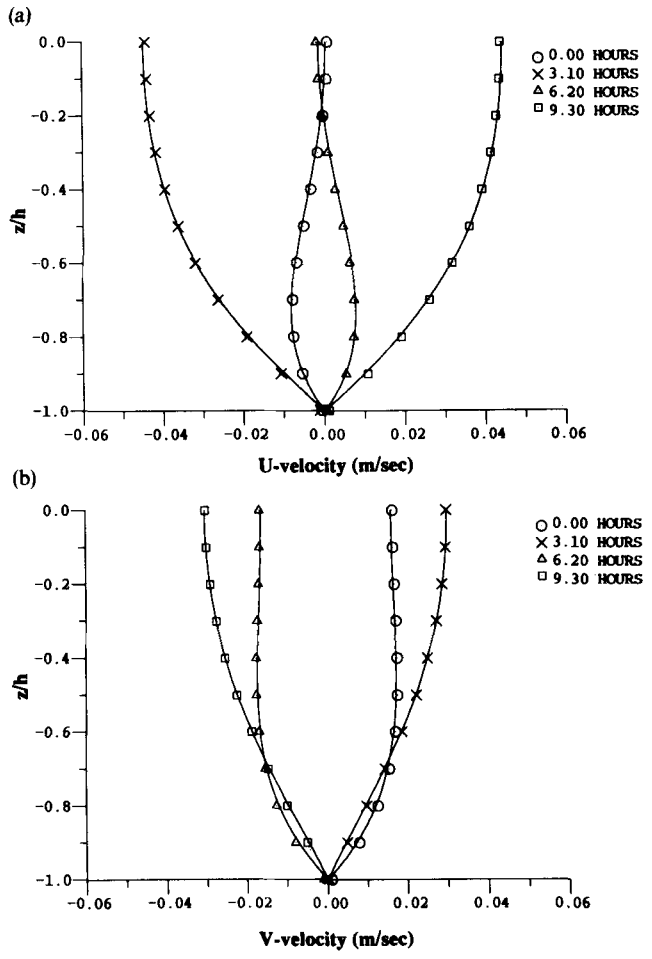

Figure 7. Exact (solid lines) and numerical velocity profiles at four points in time, at mesh point A in Figure 3: (a) x-velocity; (b) y-velocity

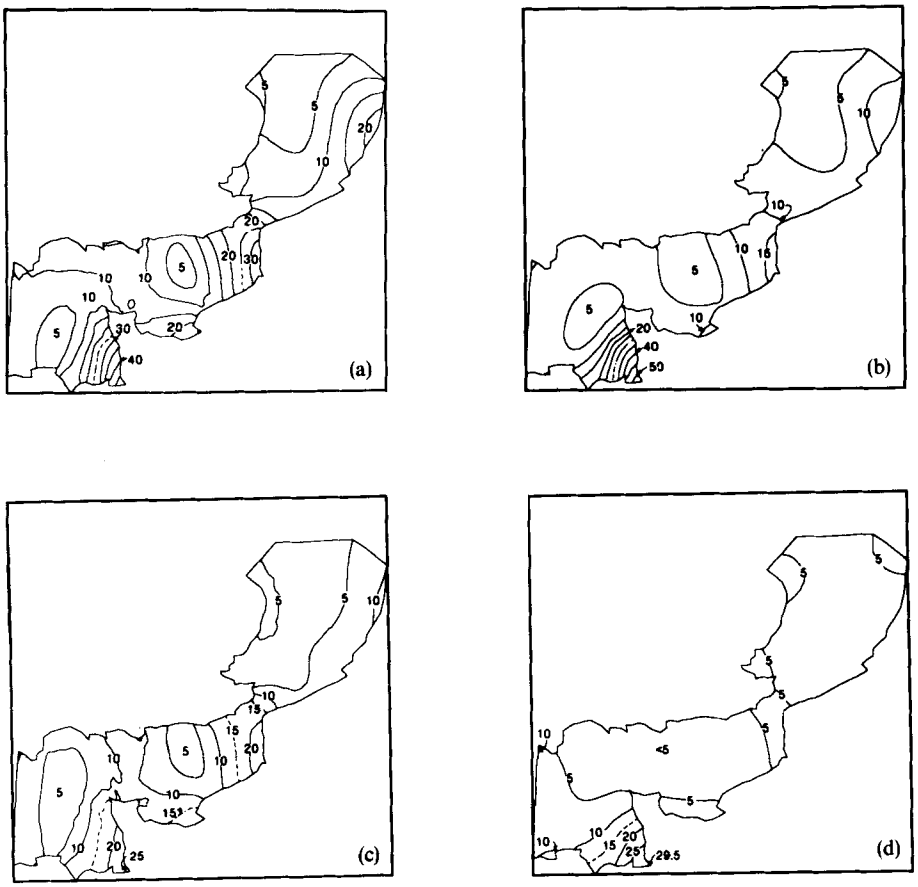

Figure 8. Co-amplitude plots of the M_4 tide in the English Channel/Southern Bight model, computed with $(N_0, \kappa) = (0{\cdot}2, 0{\cdot}005)$: (a) fully non-linear response; (b) convective terms deleted; (c) wave drift terms deleted; (d) both convective and wave drift terms deleted. Amplitudes are in centimeters

essentially equivalent in quality to that reported in Reference 1 for the harmonic model. (In these and all subsequent results the two numerical parameters θ and τ_0 are set at 0·75 and $2{\cdot}0 \times 10^{-4}$ s^{-1} respectively.)

As a test of the non-linear behaviour of our model we have recomputed the barotropic tides in the English Channel/Southern Bight using the same horizontal mesh studied previously.[5,10] In computing the 3D response we used 14 equally spaced vertical elements and a quadratic bottom stress, equation (34). Following Davies,[13] we used a vertically homogeneous viscosity proportional to the square of the local vertically averaged velocity:

$$N = N_0 |\bar{\mathbf{v}}|^2. \tag{38}$$

For test purposes we simulated only the M_2, M_4 and M_6 constituents in order to obtain the main internal M_4 interactions, as in Reference 14, and experimented with removing the convective and wave drift* terms. The simulation was run for an integral number of M_2 periods, and once in

* Product of ζ and $\mathbf{v}$ in the vertically averaged equations, and the geometric effects of time-dependent vertical mesh stretching in the momentum equation.

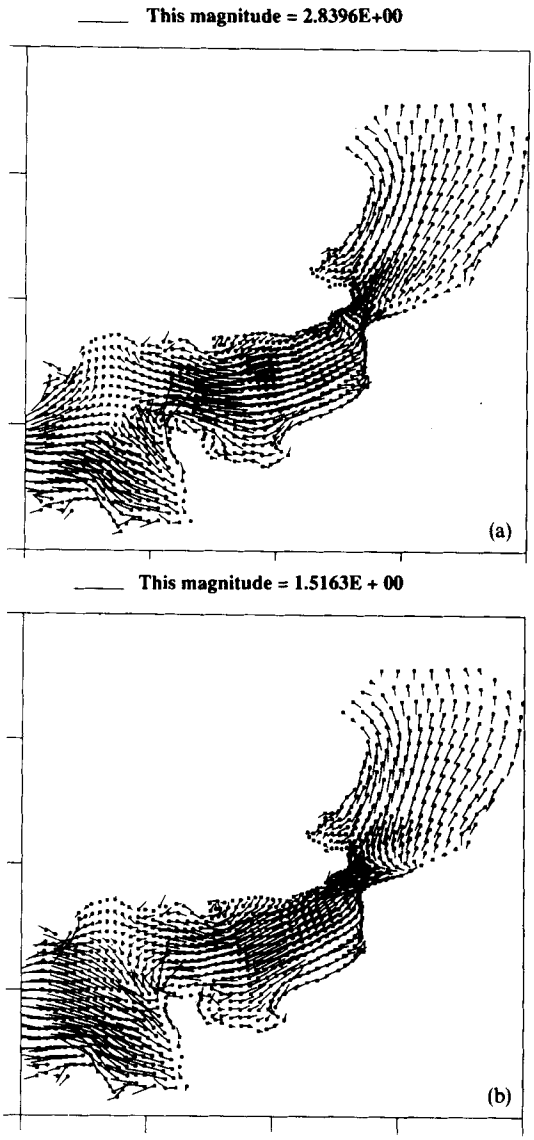

Figure 9. Velocity (m s^{-1}) in the Channel/Bight model forced by 11 constituents at 10:35 on 17 March 1976: (a) surface; (b) two elements above the bottom

dynamic steady state the three constituents were recovered by Fourier transform of the computed time series. The fully non-linear 3D solution with $(N_0, \kappa) = (0.2, 0{\cdot}005)$ generally gave elevation results in agreement with available data (e.g. Reference 15) and with previous 2D runs. Cotidal charts for M_4 appear in Figure 8, where we also show the same result obtained with the convective and/or wave drift terms deleted. It is clear that both terms contribute significantly to the M_4 result and that without both mechanisms this constituent cannot be properly represented even in a relatively limited-area study such as this. Similar findings were reached by Pingree and

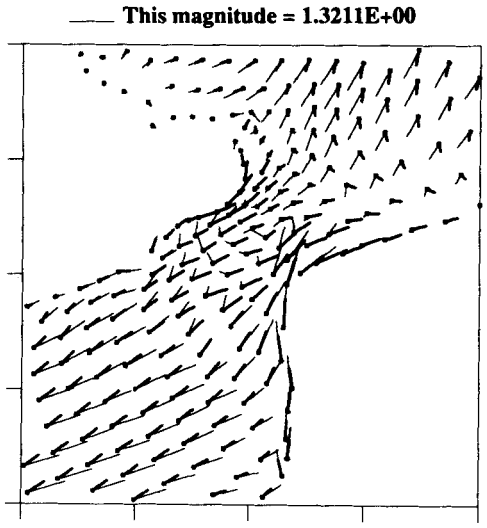

Figure 10. Detail of Figure 9 in the Strait of Dover: thin, surface velocities; thick, velocity two elements above the bottom

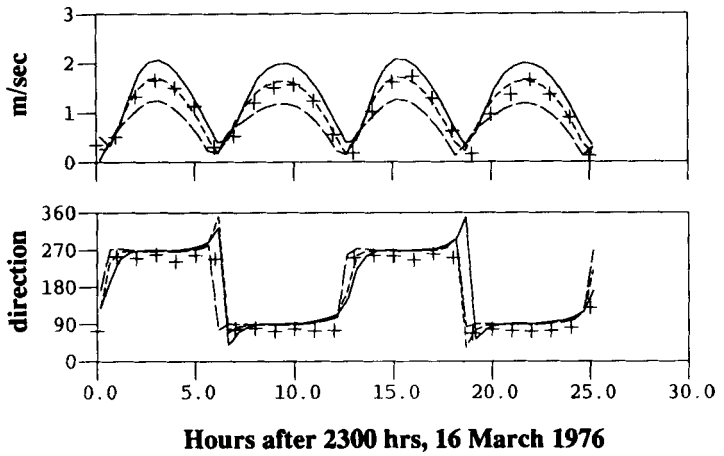

Figure 11. Comparison of velocity data (crosses) and model results at station 3 in the English Channel, south of Christchurch. Model results are plotted for the surface (solid line), near the depth of the current meter (21·2 m; short-dash line) and two levels above the bottom (long-dash line). The measured depth was 43 m, the current meter was at 20 m and the model bathymetry was 37·11 m

Maddock[16] and Walters and Werner,[14] and we take this as partial confirmation that the non-linearities are properly captured in the present model.

In Figures 9 and 10 we show the surface and bottom velocities for a comparable non-linear run forced by all 11 constituents on the boundary. Significant veering at depth is evident, due in part to the dynamics of flow reversal occurring at this point in time. In Figure 11 we compare the computed velocity time series with available data at station 3 in the Channel (south of

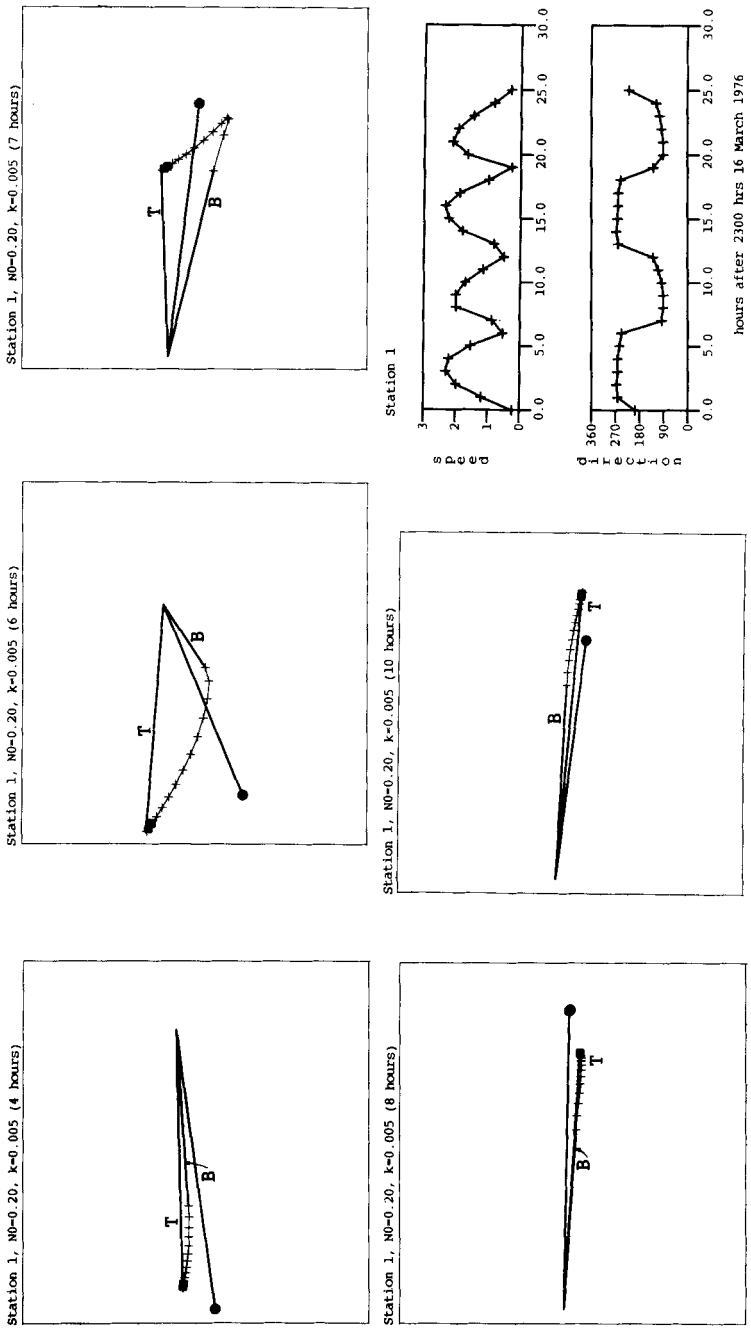

Figure 12. Computed hodographs at velocity station 1 in the English Channel (north of Cherbourg) beginning at 23:00 on 16 March 1976. The velocity is in m/s^{-1}. Vertical mixing parameters are $(N_0, \kappa) = (0{\cdot}2, 0{\cdot}005)$. The surface and bottom vectors are indicated by T (top) and B (bottom) respectively; interior nodal vectors are marked with the plus signs. The measured velocity is indicated by the vector terminated by a circle. The corresponding depth of measurement is bracketed by the squares on the computed hodograph. Also shown are speed and direction versus time for the observations

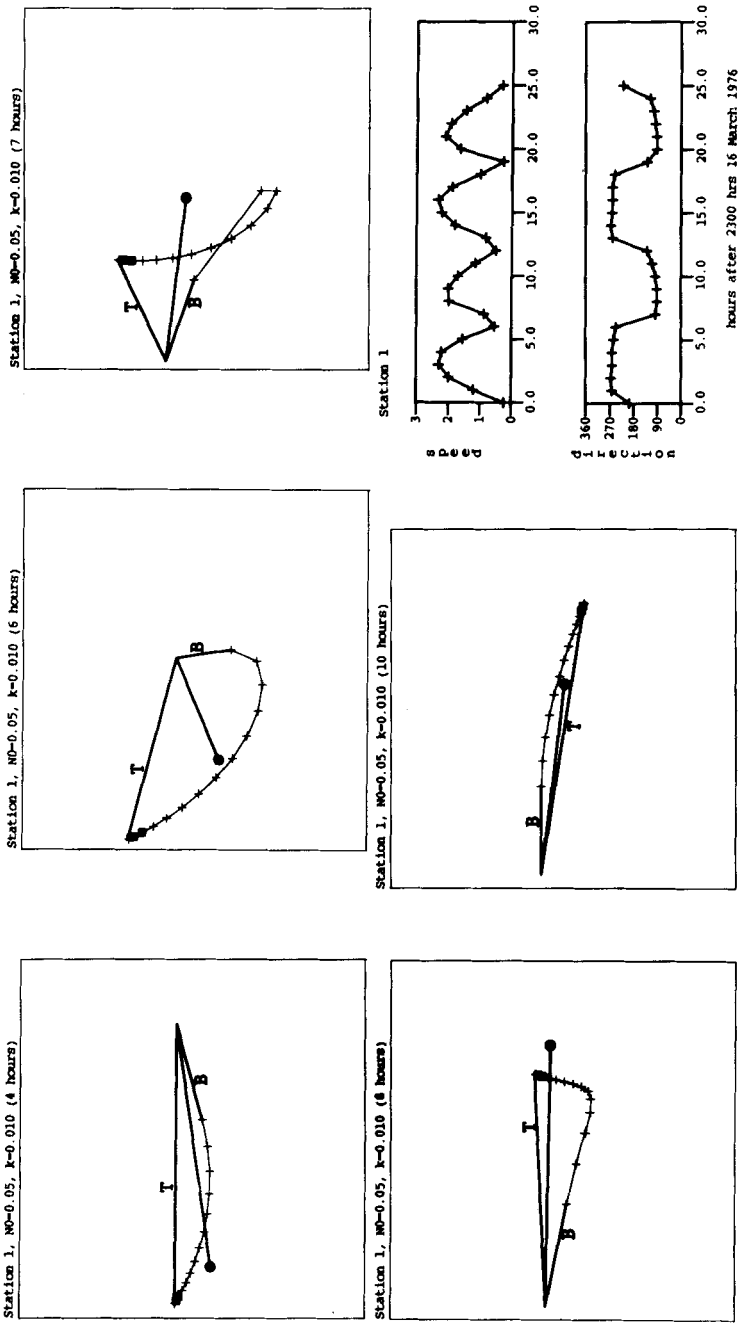

Figure 13. Same as Figure 12 but with $(N_0, \kappa)=(0{\cdot}05, 0{\cdot}01)$

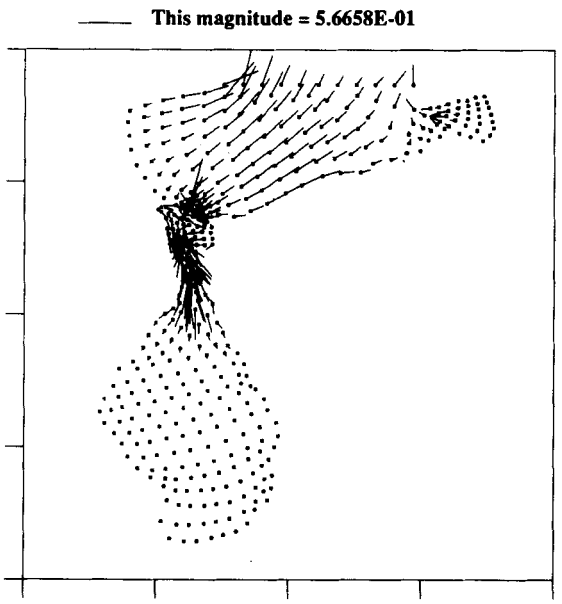

Figure 14. Computed surface velocities (m s^{-1}) in the Lake Maracaibo system, illustrating the basic semidiurnal co-oscillation: ebbing in the Gulf of Venezuela concurrent with flooding in the lake. The simulation began at 00:00 on 15 March 1976. Elapsed time is 60·5 h; the time step is 6 min; $(N_0, \kappa)=(0{\cdot}1, 0{\cdot}005)$

Christchurch), and in Figures 12 and 13 we show example hodograph series computed at station 1 (north of Cherbourg) along with the observations at depth. The two pairs of vertical shear parameters give similar elevation results, but the velocity profiles are quite different. (For further details see Reference 17.)

As a third example we have revisited the Lake Maracaibo system, studied earlier with the harmonic model.[1] Since then we have completely revised the geometry and boundary conditions and completed a non-linear study involving the simulation of 11 coupled tidal constituents over a 40-day period. In this case the full non-linear model was used, with quadratic bottom stress and vertical viscosity proportional to $|\bar{v}|^2$ as above and 14 equally spaced vertical elements everywhere. A representative plot of the surface velocity appears in Figure 14, illustrating the basic co-oscillation of the Gulf of Venezuela and the lake. Computed velocity hodograph series at representative points in the gulf and the Strait of Maracaibo are shown in Figures 15 and 16. The gulf hodographs show relatively uniform velocities in the upper layers and a bottom Ekman layer. The strait hodographs show greater vertical mixing owing to the high tidal velocities and shallow depths. The characteristic tidal phase lead at depth is clearly present in both series, although the strait flow is nearly unidirectional, being confined by the narrow geometry. (See Reference 18 for details.)

Finally, we present some speculative results aimed at the longer-term circulation in Lake Maracaibo. Using the same finite element mesh as above and based on the physical description in Reference 19, the effects of wind and density gradient were simulated separately in the absence of tides. The viscosity N was set at the constant value of 0·01 $m^2 s^{-1}$ to approximately compensate for the absence of tides; the non-linear bottom stress parameter κ was set at 0·1. In Figure 17 we illustrate the response to a steady, uniform wind stress at 1 dyn cm^{-2}, directed from the northeast,

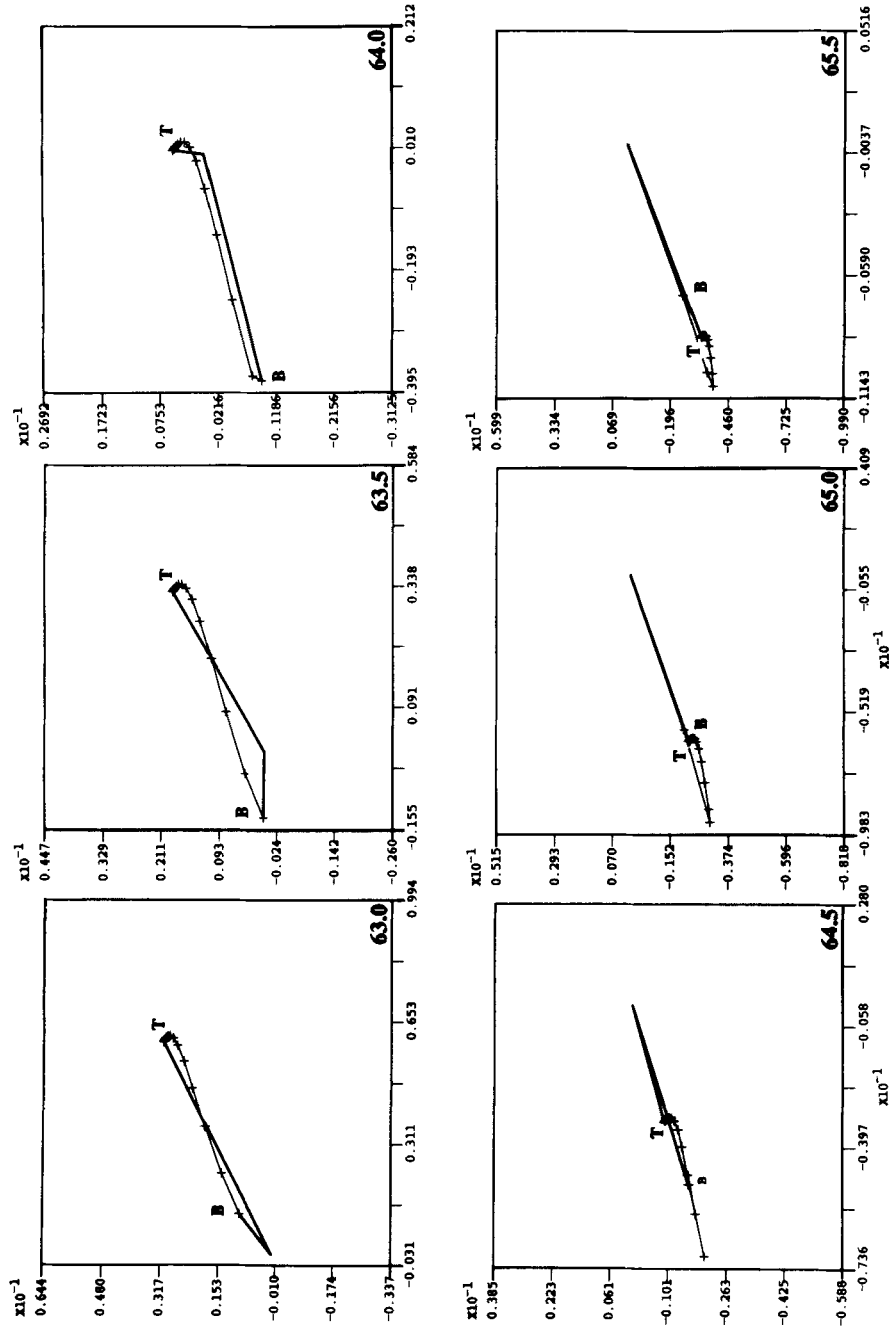

Figure 15. Computed hodograph series (m s^{-1}) at a representative point in the Gulf of Venezuela. Elapsed time is indicated in hours. $(N_0, \kappa) = (0{\cdot}1, 0{\cdot}005)$. The surface and bottom vectors are indicated by T and B respectively; interior vectors are marked by the plus signs on the hodograph

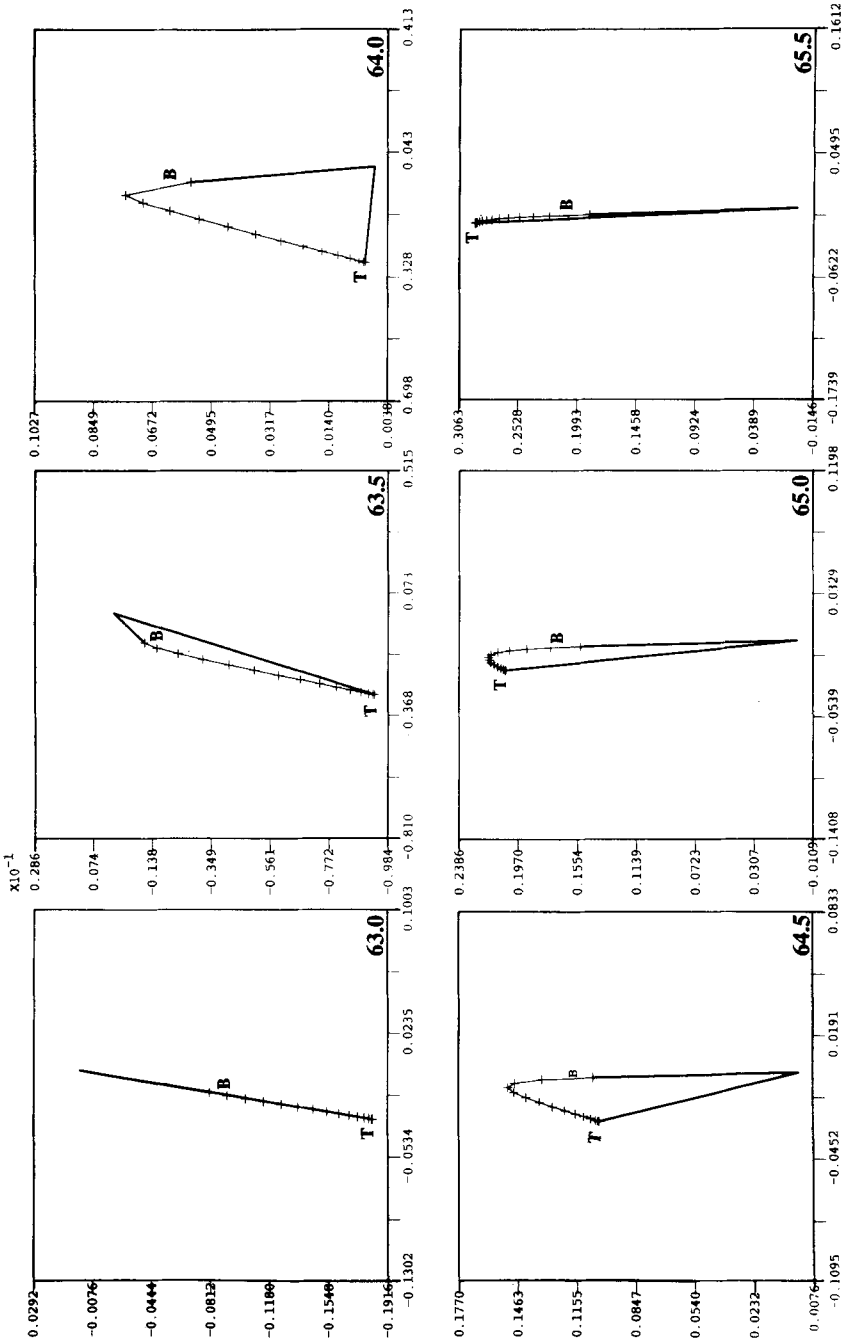

Figure 16. Same as Figure 15 for a representative point in the Strait of Maracaibo

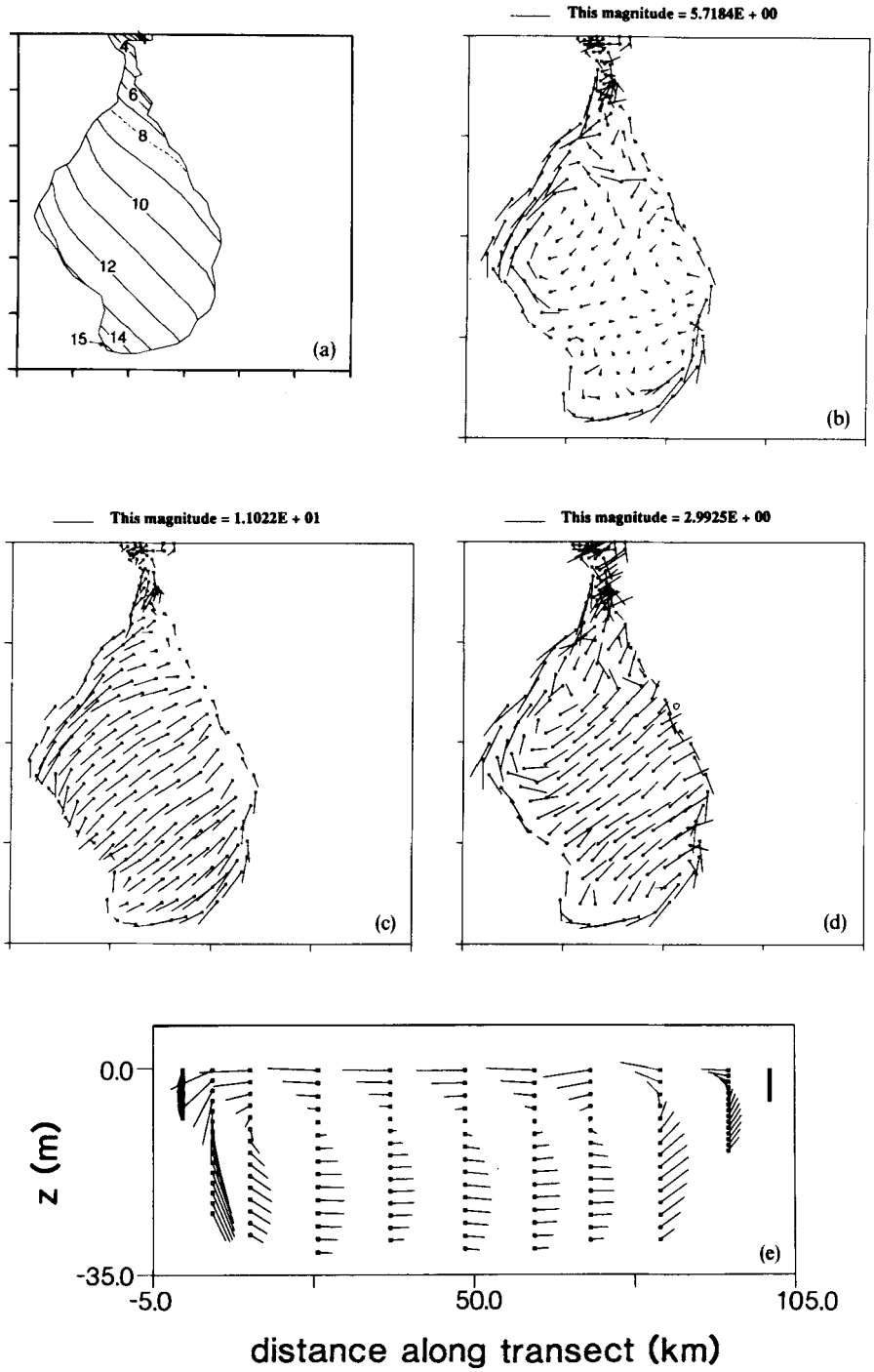

Figure 17. Steady response of Lake Maracaibo to uniform wind from the northeast: (a) surface elevation; (b) vertically averaged velocity; (c) surface velocity; (d) velocity at the bottom; (e) horizontal and vertical velocities along transect indicated in Figure 18 (the horizontal velocities were rotated into the along-transect direction; the maximum horizontal velocity is 3·9 cm s^{-1}, the maximum vertical velocity is 0·0029 cm s^{-1}). Elevation is in centimeters, velocity in cm s^{-1}

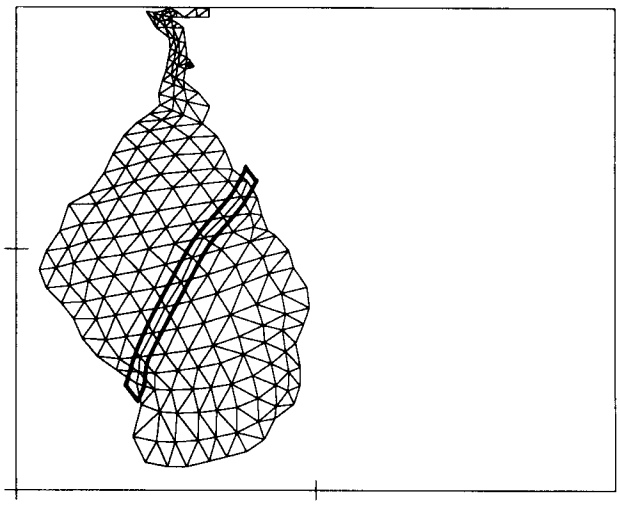

Figure 18. Transect across the Lake Maracaibo basin used to display horizontal and vertical velocity fields in Figures 17(e) and 19(e)

following a 10-day spin-up. The circulation pattern is qualitatively the same as that computed earlier with our linearized model,[1] with weaker velocities owing to the higher viscosity used here. Figure 17(e) shows the cross-basin horizontal and vertical velocities along the transect of Lake Maracaibo indicated in Figure 18. The circulation resembles that of an enclosed basin with no rotation: the surface layer flow is approximately in the direction of the wind, it downwells at the southwest shore, returns at depth and upwells at the northeast shore. In Figure 19 we show the steady response to an externally imposed density field, approximating dense water at the centre and bottom of the basin—idealizing the observed structure of the lake's cone-shaped hypolimnion. The surface density ρ_s is given by

$$\rho_s = \rho_0 + \Delta\rho \cos\left(\frac{\pi}{2}\frac{R}{R_0}\right), \tag{39}$$

with $\Delta\rho = 0{\cdot}0012\ \mathrm{g\,cm^{-3}}$ and $R_0 = 80$ km. (For $R > R_0$, $\rho_s = \rho_0$.) Internally, ρ varies linearly with depth, to a maximum of $\rho_0 + \Delta\rho$ at 30 m. The resulting circulation in Figure 19 is weak, with convergence at the surface (Figure 19(c)), divergence at the bottom (Figure 19(d)) and compensating vertical motions sinking at the centre of the lake and upwelling at the edges (Figure 19(e)). There is some numerical distress near the shore, reflecting an unphysical combination of topography and the imposed density field. Additionally, the near-shore upwelling patterns reveal the coarseness of the mesh relative to both the flow and the bathymetric slopes. Overall, viscosity and topography dominate over rotation in this solution. The results of Figure 19 suggest that the observed density field cannot sustain itself in geostrophic balance with the currents. Similar experiments with either higher rotation representative of mid-latitude or lower viscosity produced a more classical gyre-like surface response with the viscous features confined to the lower depths. These results are strictly exploratory; investigation of the physics of this system is continuing.

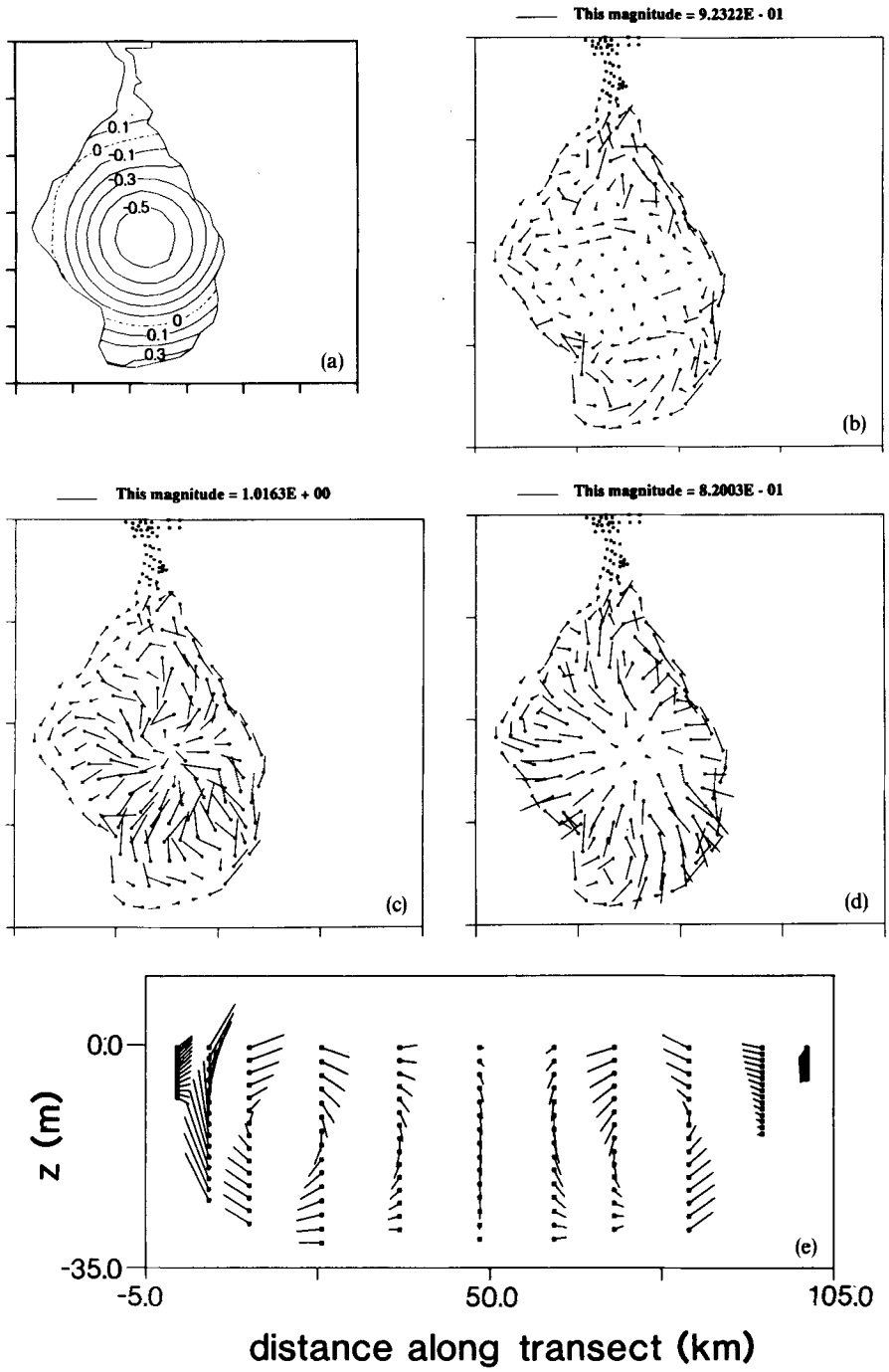

Figure 19. Steady response of Lake Maracaibo to prescribed hypothetical density field: (a) surface elevation; (b) vertically averaged velocity; (c) surface velocity; (d) velocity at the bottom; (e) horizontal and vertical velocities along transect indicated in Figure 18 (the horizontal velocities were rotated into the along-transect direction; the maximum horizontal velocity is 0·68 cm s^{-1}, the maximum vertical velocity is 0·0013 cm s^{-1}). Elevation is in centimeters, velocity in cm s^{-1}

6. CONCLUSIONS

The basic hydrodynamic framework presented here has several desirable features in the context of continental shelf circulation modelling.

1. The finite element method in the horizontal facilitates resolution of detailed coastal and bathymetric features.
2. The use of deforming finite elements through the vertical provides flexibility in vertical discretization which may evolve during the course of simulation.
3. The simple 3D linear elements used here allow pre- and postprocessing to be achieved within the simpler 2D paradigm.
4. The use of the wave equation form of the governing equations eliminates spurious gravity waves on simple elements without artificial horizontal viscosity.
5. The semi-implicit time-stepping algorithm uncouples the elevation and velocity computations.
6. Nodal quadrature tridiagonalizes the velocity calculations such that the entire calculation scales as a 2D gravity wave algorithm.
7. Full flexibility for arbitrary variations in vertical mixing is preserved.

This non-linear model is generally compatible with its linearized harmonic predecessor, which may be used in preliminary studies and as an initial condition generator with the same mesh. The model tests well against linear analytic solutions and in two field studies to date. Its further development into a full-featured continental shelf model, including the incorporation of turbulence closure and concurrent simulation of density field evolution, is recommended.

ACKNOWLEDGEMENTS

This work was supported by the National Science Foundation, Grants CEE-8352226 and INT-8514156.

REFERENCES

1. D. R. Lynch and F. E. Werner, 'Three-dimensional hydrodynamics on finite elements. Part I: Linearized harmonic model', *Int. j. numer. methods fluids*, **7**, 871–909 (1987).
2. D. R. Lynch, F. E. Werner, D. A. Greenberg and J. W. Loder, 'A diagnostic model for baroclinic and wind-driven circulation in shallow seas', *Continental Shelf Research* (submitted).
3. D. R. Lynch and W. R. Gray, 'A wave equation model for finite element tidal computations', *Comput. Fluids*, **7**, 207–228 (1979).
4. F. E. Werner and D. R. Lynch, 'Meeting report: 2nd Tidal Flow Forum', *EOS*, **69**, 1027–1028 (1988).
5. F. E. Werner and D. R. Lynch, 'Harmonic structure of English Channel/Southern Bight tides from a wave equation simulation', *Adv. Water Resources*, **12**, 121–142 (1989).
6. W. G. Gray, J. Drolet and I. P. E. Kinnmark, 'A simulation of tidal flow in the southern part of the North Sea and the English Channel', *Adv. Water Resources*, **10**, 131–137 (1987).
7. R. A. Walters, 'A model for tides and currents in the English Channel and southern North Sea', *Adv. Water Resources*, **10**, 138–148 (1987).
8. B. M. Jamart and J. Ozer, 'Some results and comments on the Tidal Flow Forum exercise,' *Advances in Water Resources*, **12**, 211–220 (1989).
9. I. P. E. Kinnmark, 'The shallow water equations: formulation, analysis and application', in C. A. Brebbia and S. A. Orszag (eds), *Lecture Notes in Engineering, Vol. 15*, Springer-Verlag, Berlin, 1985, 187 pp.
10. F. E. Werner and D. R. Lynch, 'Field verification of wave equation tidal dynamics in the English Channel and southern North Sea', *Adv. Water Resources*, **10**, 115–130 (1987).
11. J. R. Westlake, *A Handbook of Numerical Matrix Inversion and Solution of Linear Equations*, Krieger, Huntington, NY, 1975.

12. D. R. Lynch and C. B. Officer, 'Analytic test cases for 3-D hydrodynamic models', *Int. j. numer. methods fluids*, **5**, 529–543 (1985).
13. A. M. Davies, 'A three-dimensional model of the northwest European continental shelf with application to the M_4 tide', *J. Phys. Oceanogr.*, **16**, 797–813 (1986).
14. R. A. Walters and F. E. Werner, 'A comparison of two finite element models using the North Sea data set', *Adv. Water Resources*, **12**, 184–193 (1989).
15. M. M. G. Chabert D'Hieres and C. Le Provost, (1979) 'Atlas des composantes harmoniques de la marée dans La Manche', *Ann. Hydrogr.*, **6**, 5–36 (1979).
16. R. D. Pingree and L. Maddock, 'The M_4 tide in the English Channel derived from a non-linear numerical model of the M_2 tide', *Deep Sea Res.*, **25**, 53–63 (1978).
17. D. R. Lynch and F. E. Werner, 'Three-dimensional velocities from a finite element model of English Channel/southern bight tides', in B. Parker (ed.), *Tidal Hydrodynamics*, John Wiley & Sons, NY, (1990) in press.
18. D. R. Lynch, F. E. Werner, J. M. Molines and M. Fornerino, 'Tidal hydrodynamics in a coupled ocean/lake system', *Estuar., Coastal, Shelf Sci.*, (1990) in press.
19. G. Parra-Pardi *et al. Estudio Integral sobre la Contaminación del Lago de Maracaibo y sus Afluentes. Parte II: Evaluación del Proceso de Eutrificación*, Ministerio del Ambiente y de los Recursos Naturales Renovables, DISCA, Caracas, Venezuela, 1979.